Research Square

Preprints are preliminary reports that have not undergone peer review.
They should not be considered conclusive, used to inform clinical practice,
or referenced by the media as validated information.

From point electrostatic sources to extended electrostatic architectures near Lagrange points

Vladimir Aslanov
Moscow Aviation Institute
Juan Antonio Vera
juanantonio.vera@upct.es
Universidad Politécnica de Cartagena

Research Article

Keywords: Restricted three-body problem, Electrostatic interaction, Artificial equilibria, Bifurcations, Spectral stability, Mars–Phobos

Posted Date: November 9th, 2026

DOI: https://doi.org/10.21203/rs.3.rs-11402046/v1

License: This work is licensed under a Creative Commons Attribution 4.0 International License.
Read Full License

Additional Declarations: No competing interests reported.

From point electrostatic sources to extended electrostatic architectures near Lagrange points

Vladimir S. Aslanov[1] and Juan A. Vera[2*]

[1]Professor, Department of Applied Mathematics 921, Moscow Aviation Institute (National Research University), 4, Volokolamskoe Shosse, A-80, GSP-3, Moscow, Russia. E-mail: aslanov_vs@mail.ru; URL: http://aslanov.ssau.ru/.

[2]Associate Professor, Department of Applied Mathematics and Statistics, Universidad Politécnica de Cartagena, Paseo Alfonso XIII, 52, 30203, Cartagena, Spain.

*Corresponding author(s). E-mail(s): juanantonio.vera@upct.es;

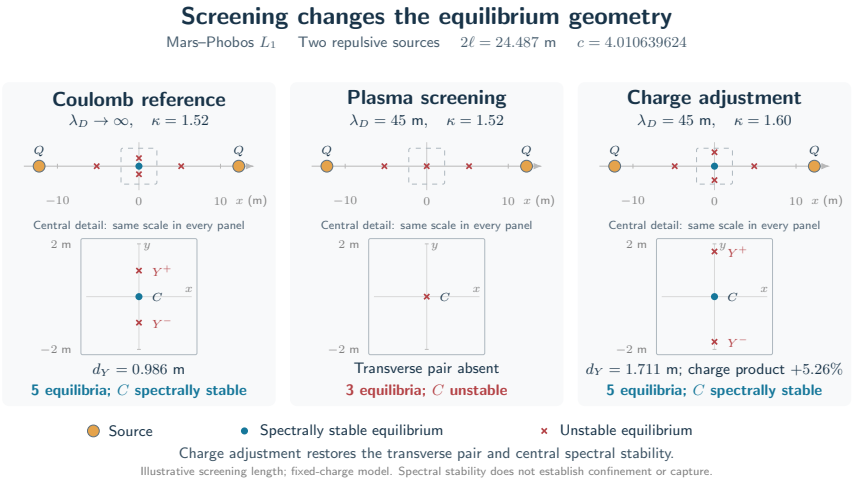
Abstract

Electrostatic forces can modify the motion of a charged body near a collinear libration point in the circular restricted three-body problem (CRTBP). This study examines how two equal repulsive sources placed symmetrically about this point affect the number, spatial arrangement, and stability of equilibria. The local model combines a quadratic approximation of the gravitational field with the full unscreened electrostatic potential of the sources. After nondimensionalization and parameter reduction, the model depends on two parameters: the local gravitational curvature and the reduced charge strength. Explicit expressions describe the equilibrium branches along the three coordinate axes and identify the critical parameter values at which bifurcations occur.

The analysis also examines how Debye screening changes the equilibrium configuration, bifurcations, and local dynamics, and how a small charge asymmetry displaces the central equilibrium from the midpoint. A numerical example in the Mars–Phobos system illustrates the relationship between stability and equilibrium separation. The critical Jacobi levels are computed, and conjectures concerning the model's nonlinear dynamics are discussed.

These results provide a basis for further studies of local motion and controlled insertion. Nonlinear confinement and finite-conductor effects require further investigation, while asymptotic capture requires additional dissipative or feedback mechanisms.

Graphical abstract



Keywords: Restricted three-body problem, Electrostatic interaction, Artificial equilibria, Bifurcations, Spectral stability, Mars–Phobos

1 Introduction

Keeping a small capsule near a collinear libration point is a possible task in a sample-return mission. However, these points are unstable in the circular restricted three-body problem (CRTBP): small disturbances can move the capsule away. Electrostatic forces offer a way to change its motion without mechanical contact. Schaub, Parker and King (Schaub et al. 2004) discussed the opportunities and practical challenges of controlling close spacecraft formations through electric forces. Aslanov and Schaub (Aslanov and Schaub 2019) studied the use of an electrostatic pusher to reduce the rotation of a nearby body. These works provide a basis for considering electric forces in local spacecraft operations.

The broader idea of changing equilibrium positions through an applied force has also been studied in the three-body problem. McInnes and co-authors (McInnes et al. 1994) examined solar sail parking in this setting. Bombardelli and Peláez (Bombardelli and Peláez 2011) analysed the stability of artificial equilibria with minimum control acceleration. Aliasi, Mengali and Quarta (Aliasi et al. 2011) studied the positions and linear stability of equilibria for a general sail model. These studies show why both the form of the applied force and the stability of the resulting positions matter for mission design.

More directly related to the present problem, Aslanov (Aslanov 2021b) studied how an attractive electrostatic source splits a collinear libration point into additional equilibria. In a related mission study, he considered the delivery of a charged Phobos sample container to the vicinity of an orbiter (Aslanov 2021a). These studies

connect local equilibrium changes with a possible sample-return operation. The additional equilibria can still be unstable. This raises a further question: how does the arrangement of the sources affect the positions and stability of the equilibria?

This paper considers two equal repulsive sources placed at equal distances on opposite sides of a collinear libration point. The sources lie along the line joining the two primary bodies. Their electric forces cancel at the midpoint. Near this point, the electric force pushes the capsule back towards the midpoint along the source line, but away from this line in the perpendicular directions. Stability therefore depends on the combined effects of the electric field, gravity and rotation. The local model uses a quadratic approximation of the gravitational potential and the full unscreened electrostatic potential of both sources. After scaling, two parameters describe the model: the local gravitational curvature and the reduced charge strength.

The analysis gives explicit positions for all equilibria of this unscreened local model. They lie at the centre or in pairs along three directions: the source line, the perpendicular direction in the orbital plane, and the direction normal to that plane. As the charge strength increases, the number of distinct equilibria changes from three to five, then to seven and back to five, away from the transition values. The transverse and vertical pairs appear at the centre, while the longitudinal pair later merges with it and disappears. These results describe how the electric field changes the local arrangement of possible resting positions.

The central equilibrium supports bounded small oscillations in all three directions within a narrow range of charge strength in the linear model. The width of this range, measured in the reduced charge parameter, is independent of the gravitational curvature. A second range allows bounded linear motion in the orbital plane, but disturbances perpendicular to the plane grow. Thus, increasing the charge strength does not always improve stability. All secondary equilibria are unstable in space. The transverse pair has one growing direction, whereas the longitudinal pair has an additional vertical instability. These differences matter when considering possible approach and departure paths.

Two changes to the ideal symmetric model are also examined. Debye screening reduces the range of the electric interaction. Seubert, Stiles and Schaub (Seubert et al. 2014) examined how plasma conditions affect electric force estimates for spacecraft in Earth orbit. Their work motivates checking the sensitivity to screening here, while the local conditions near Phobos require separate assessment. In the Mars–Phobos example, it can remove the transverse pair and destroy central linear stability, even when the longitudinal positions change only slightly. A modest increase in the charge product restores the transverse pair and central linear stability in the screened case studied here. The chosen screening length is illustrative and requires comparison with local plasma conditions. Separately, a small difference between the source charges shifts the central equilibrium along the source line. The analysis gives its leading displacement away from the transition where the longitudinal pair merges with the centre.

Periodic orbits and the paths around them provide a further link to mission design. Conley (Conley 1968) studied low-energy transit orbits in the restricted three-body

problem. Richardson (Richardson 1980) developed analytical approximations for periodic orbits near collinear points. Koon and co-authors (Koon et al. 2001) used the paths that approach and leave such orbits to study low-energy transfers to the Moon. These works provide a framework for later transport studies in the present electrostatic model.

The Mars–Phobos application connects the equilibrium results to physical distances. In the case with central spatial linear stability, the transverse points are about one metre from the midpoint. In the case with stronger charge, they are about six metres away, but the centre is vertically unstable. The critical Jacobi levels identify changes in the regions where the energy constraint permits motion. A small periodic orbit near a transverse equilibrium is also computed, together with a check of how nearby planar paths separate from it. These calculations describe local motion; a complete approach path still has to be found. Comparison with the full CRTBP gravitational field gives only small shifts of the secondary equilibria at the adopted scale. It leaves the central linear stability unchanged for the same symmetric, fixed sources.

These results can guide an initial mission geometry. A possible layout would place two charged units on opposite sides of the target point, with free space near their midpoint and along the intended approach path. The equilibrium positions can then be compared with the capsule size, electrodes, supporting structures and required clearance. For example, the transverse points in the lower-charge case lie inside the illustrative two-metre exclusion radius used here. The stronger-charge case puts all four secondary planar points outside that radius, but loses central vertical stability. If a solid spacecraft body occupies the midpoint, the central equilibrium is also inaccessible. Source spacing and charge must therefore be chosen together with the material layout. The present results provide an initial check of such choices; they do not yet validate an operational mission design.

Several questions about nonlinear motion remain for a later theoretical study. Bounded linear oscillations do not prove that a capsule stays near the centre for a long time. Interactions between oscillations may change the motion when their frequencies become equal or are related by simple ratios. At the upper edge of the spatial stability range, two planar frequencies become equal. Further analysis must determine whether new periodic orbits appear there and whether they are stable. The simultaneous change in planar and vertical motion when the vertical pair appears also needs a separate spatial analysis. Other open questions include the effect of larger disturbances, the stability of periodic orbits outside the orbital plane, and the size of any region of bounded motion. The paths that approach and leave unstable equilibria and periodic orbits must be followed to test whether they connect useful mission locations without collisions. The earlier transport studies provide methods for this task, but the connections must be established for the electric field and geometry considered here.

Physical extensions should include finite electrodes and the redistribution of charge on nearby conductors. Stevenson and Schaub (Stevenson and Schaub 2013) introduced the Multi-Sphere Method to estimate electric forces and torques for conducting bodies of different shapes. This provides one possible way to include the material geometry in a future model. Plasma conditions that vary in space and time should also be considered. The motion and attitude of the source spacecraft, and the control needed

to maintain their positions, should also be included. Further work can examine unequal or differently arranged sources and continue the local orbits in the full gravitational field. Finally, placing a capsule near a selected orbit and making it settle there are different tasks. The fixed conservative field cannot make an open range of initial states converge to a stable resting point. Asymptotic capture therefore requires an additional dissipative or feedback mechanism.

Section 2 introduces the model, and Section 3 derives the equilibrium branches. Section 4 studies their linear stability. Section 5 presents the Mars–Phobos application, followed by the discussion and conclusions.

2 Electrostatic model in the circular restricted three-body problem

This section introduces the local model used throughout the paper. It combines the circular restricted three-body problem (CR3BP) near an arbitrary collinear libration point with a symmetric two-source electrostatic configuration (Fig. 1). The resulting reduced model retains the local gravitational curvature while isolating the effect of the electrostatic strength.

Consider two primaries of masses m_1 and m_2 moving on circular orbits about their centre of mass, and a third body of negligible mass. Let a be the distance between the primaries and n their orbital angular velocity. Define

$$\mu = \frac{m_2}{m_1 + m_2}, \qquad 0 < \mu \leq \frac{1}{2}.$$

The standard CR3BP normalization uses a as the unit of length, $m_1 + m_2$ as the unit of mass, and n^{-1} as the unit of time. In the barycentric rotating frame (x, y, z), the primaries are located at

$$P_1 = (-\mu, 0, 0), \qquad P_2 = (1 - \mu, 0, 0),$$

and the dimensionless effective potential is

$$\Omega_0(x, y, z) = \frac{1}{2}(x^2 + y^2) + \frac{1 - \mu}{r_1} + \frac{\mu}{r_2},$$

where

$$r_1^2 = (x + \mu)^2 + y^2 + z^2,$$
$$r_2^2 = (x - 1 + \mu)^2 + y^2 + z^2.$$

The equations of motion are

$$\ddot{x} - 2\dot{y} = (\Omega_0)_x,$$
$$\ddot{y} + 2\dot{x} = (\Omega_0)_y,$$
$$\ddot{z} = (\Omega_0)_z.$$

Let

$$L_i = (x_{L_i}, 0, 0), \qquad i = 1, 2, 3,$$

be any of the three collinear libration points. The dimensionless distances from L_i to the primaries are

$$r_{1,L_i} = |x_{L_i} + \mu|, \qquad r_{2,L_i} = |x_{L_i} - 1 + \mu|,$$

and the local gravitational curvature is defined by

$$\boxed{c_i = \frac{1-\mu}{r_{1,L_i}^3} + \frac{\mu}{r_{2,L_i}^3}}.$$

The collinear CR3BP equations give $c_i > 1$ for $i = 1, 2, 3$. Thus, this inequality is a property of the underlying CR3BP and not an additional restriction of the electrostatic model.

Let 2ℓ be the dimensional separation between the electrostatic sources and define

$$\epsilon = \frac{\ell}{a}.$$

Using local coordinates scaled with ℓ,

$$x = x_{L_i} + \epsilon X, \qquad y = \epsilon Y, \qquad z = \epsilon Z.$$

Since L_i is an equilibrium, the linear term in the Taylor expansion vanishes. The Hessian of the CR3BP potential at a collinear point is

$$D^2\Omega_0(L_i) = \begin{pmatrix} 1+2c_i & 0 & 0 \\ 0 & 1-c_i & 0 \\ 0 & 0 & -c_i \end{pmatrix}.$$

Hence,

$$\Omega_0 = \Omega_0(L_i) + \epsilon^2\Omega_2(X, Y, Z) + O(\epsilon^3),$$

where

$$\Omega_2(X, Y, Z) = \tfrac{1}{2}(1+2c_i)X^2 + \tfrac{1}{2}(1-c_i)Y^2 - \tfrac{1}{2}c_iZ^2.$$

This quadratic part defines the baseline local gravitational model; higher-order terms are examined in Section 5.6. The source charges and positions are prescribed in the rotating frame. Sample back-reaction is neglected, and the Coulomb interaction is unscreened.

2.1 Electrostatic configuration and reduced model

Two equal electrostatic sources are placed symmetrically about L_i. This is the two-source configuration considered in this work for modifying the local effective potential while keeping the system autonomous and conservative.

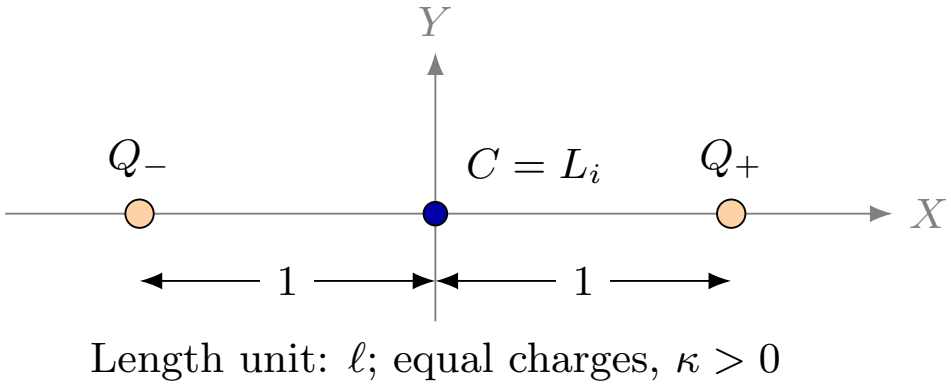


Fig. 1 Local geometry of the symmetric two-source electrostatic configuration around the reference collinear point L_i. Positions and distances are expressed in units of the half-separation ℓ

The dimensional distances from L_i to the primaries are

$$R_{1,L_i} = a\, r_{1,L_i}, \qquad R_{2,L_i} = a\, r_{2,L_i}.$$

The parameter

$$\varepsilon_i = \frac{\ell}{\min\{R_{1,L_i}, R_{2,L_i}\}}$$

measures the source half-separation relative to the distance from L_i to the nearest primary. The local approximation requires

$$\boxed{\varepsilon_i \|(X, Y, Z)\| \ll 1.}$$

In coordinates scaled with ℓ, the sources are located at

$$\mathbf{r}_- = (-1, 0, 0), \qquad \mathbf{r}_+ = (1, 0, 0),$$

and the reduced distances from the particle to the sources are

$$\rho_\pm = \sqrt{(X \mp 1)^2 + Y^2 + Z^2}.$$

With ℓ as the local unit of length and n^{-1} as the unit of time, the natural acceleration scale is $n^2\ell$. The electrostatic contribution is described by the dimensionless parameter

$$\boxed{\kappa = \frac{1}{4\pi\varepsilon_0} \frac{qQ}{mn^2\ell^3}},$$

where m and q are the mass and charge of the test particle, respectively, and Q is the charge of each source. With the adopted sign convention, $\kappa > 0$ corresponds to a repulsive interaction.

After division by $n^2\ell$, the gravitational part retains the coefficients defined by c_i. The reduced local effective potential is therefore

$$\Omega(X,Y,Z;c_i,\kappa) = \Omega_2(X,Y,Z) - \kappa\left(\frac{1}{\rho_-}+\frac{1}{\rho_+}\right).$$

The local equations of motion are

$$\begin{aligned} X'' - 2Y' &= \Omega_X, \\ Y'' + 2X' &= \Omega_Y, \\ Z'' &= \Omega_Z. \end{aligned}$$

where primes denote derivatives with respect to the dimensionless time nt.

The system is autonomous. With

$$p_X = X' - Y, \qquad p_Y = Y' + X, \qquad p_Z = Z',$$

the Hamiltonian is

$$H = \tfrac{1}{2}(p_X^2 + p_Y^2 + p_Z^2) + Yp_X - Xp_Y + \tfrac{1}{2}(X^2+Y^2) - \Omega.$$

and the Jacobi integral is

$$\boxed{\mathcal{C}_\ell = 2\Omega - (X'^2 + Y'^2 + Z'^2), \qquad \mathcal{C}_\ell = -2H.}$$

For a fixed collinear point L_i, the index i is omitted below, so that $c = c_i$. The reduced model is therefore considered for

$$c > 1, \qquad \kappa > 0.$$

3 Equilibria and bifurcations

The number and location of the equilibria determine the basic geometry of the electrostatic configuration. The following analysis describes their dependence on the reduced electrostatic strength κ and identifies the critical values at which branches appear or disappear.

For $c > 1$ and $\kappa > 0$, define

$$S = \rho_-^{-3} + \rho_+^{-3}, \qquad D = \rho_-^{-3} - \rho_+^{-3}.$$

The equilibrium condition $\nabla\Omega = 0$ can be written as

$$\begin{aligned} (1 + 2c + \kappa S)X + \kappa D &= 0, \\ Y(1 - c + \kappa S) &= 0, \\ Z(-c + \kappa S) &= 0. \end{aligned}$$

The last two equations show that Y and Z cannot both be nonzero. To exclude the remaining non-axial possibilities, take $X > 0$ by symmetry and write $b = c-1$ if $Y \neq 0$, or $b = c$ if $Z \neq 0$. Then $\kappa S = b$ and the longitudinal equation requires $-D/S = \gamma X$, where $\gamma = (1 + 2c + b)/b > 3$. Since $|D| < S$, necessarily $0 < X < 1/\gamma < 1$. For fixed X, the ratio $-D/S$ decreases with the squared transverse distance, so

$$\frac{-D}{S} \leq \frac{X(3 + X^2)}{1 + 3X^2} < 3X < \gamma X,$$

a contradiction. Thus, all regular equilibria of the unscreened model lie on the three coordinate axes.

3.1 Equilibrium branches

The central equilibrium

$$C = (0, 0, 0)$$

exists for all values of κ. The longitudinal branches are

$$X^{\pm} = (\pm X_s, 0, 0), \qquad X_s^2 = 1 - 2\sqrt{\frac{\kappa}{1 + 2c}},$$

and exist for

$$0 < \kappa < \frac{1 + 2c}{4}.$$

The transverse branches are

$$Y^{\pm} = (0, \pm Y_s, 0), \qquad Y_s^2 = \left(\frac{2\kappa}{c - 1}\right)^{2/3} - 1,$$

and exist for

$$\kappa > \frac{c - 1}{2}.$$

The vertical branches are

$$Z^{\pm} = (0, 0, \pm Z_s), \qquad Z_s^2 = \left(\frac{2\kappa}{c}\right)^{2/3} - 1,$$

and exist for

$$\kappa > \frac{c}{2}.$$

Therefore, the symmetric configuration has only the branches

$$\boxed{C, \qquad X^{\pm}, \qquad Y^{\pm}, \qquad Z^{\pm}.}$$

No additional regular equilibria with two or three nonzero coordinates are found.

3.2 Number of equilibria and critical values

Changes in the equilibrium configuration occur at

$$\kappa_1 = \frac{c-1}{2}, \qquad \kappa_2 = \frac{c}{2}, \qquad \kappa_3 = \frac{1+2c}{4},$$

with

$$\kappa_1 < \kappa_2 < \kappa_3.$$

Away from these critical values, the number of equilibria is

Interval	Equilibria	Number
$0 < \kappa < \kappa_1$	$C, X^{\pm}$	3
$\kappa_1 < \kappa < \kappa_2$	$C, X^{\pm}, Y^{\pm}$	5
$\kappa_2 < \kappa < \kappa_3$	$C, X^{\pm}, Y^{\pm}, Z^{\pm}$	7
$\kappa > \kappa_3$	$C, Y^{\pm}, Z^{\pm}$	5

As κ increases, the equilibrium configuration follows the sequence

$$\boxed{3 \longrightarrow 5 \longrightarrow 7 \longrightarrow 5.}$$

At κ_1, the transverse pair $Y^{\pm}$ appears. At κ_2, the vertical pair $Z^{\pm}$ appears. Finally, at κ_3, the longitudinal branches $X^{\pm}$ merge with the central equilibrium and disappear.

4 Linear stability and local phase-space structure

This section examines the linear stability of the unscreened equilibrium branches for $c > 1$ and $\kappa > 0$. At these points, the Hessian is diagonal. The horizontal characteristic equation is

$$\lambda^4 + (4 - \Omega_{XX} - \Omega_{YY})\lambda^2 + \Omega_{XX}\Omega_{YY} = 0,$$

and the vertical eigenvalues satisfy $\lambda_z^2 = \Omega_{ZZ}$. All derivatives are evaluated at the equilibrium.

4.1 Central equilibrium

At $C = (0, 0, 0)$, define $s = c - 2\kappa$. The curvatures are

$$A = 1 + 2s, \qquad B = 1 - s, \qquad D = -s.$$

The horizontal characteristic equation becomes

$$\lambda^4 + (2 - s)\lambda^2 + (1 + 2s)(1 - s) = 0. \tag{1}$$

Its discriminant in $u = \lambda^2$ is

$$\Delta_u = s(9s - 8). \tag{2}$$

Two distinct nonzero imaginary pairs require $2-s>0$, $(1+2s)(1-s)>0$ and $\Delta_u>0$. Thus,

$$-\frac{1}{2}<s<0 \qquad \text{or} \qquad \frac{8}{9}<s<1.$$

The two open planar stability windows are therefore

$$\frac{c-1}{2}<\kappa<\frac{c-\frac{8}{9}}{2}, \tag{3}$$

and

$$\frac{c}{2}<\kappa<\frac{c+\frac{1}{2}}{2}. \tag{4}$$

The vertical equation is $\ddot{\zeta}=-s\zeta$. Hence, only the first window also has an oscillatory vertical mode.

Proposition. The central equilibrium has three distinct nonzero imaginary eigenvalue pairs and bounded linearised motion if and only if

$$\boxed{\frac{c-1}{2}<\kappa<\frac{c-\frac{8}{9}}{2}}. \tag{5}$$

This interval has width $\Delta\kappa=1/18$, independent of c.

Figure 2 compares the two planar windows. Only the lower band also supports vertical oscillations. Increasing the electric strength beyond this band does not preserve spatial stability, even when planar stability is recovered in the upper band. The bands refer to the central equilibrium; they do not describe the stability of the secondary branches. Their boundary values are excluded.

The squared frequencies are

$$\omega_{1,2}^2=\frac{2-s\pm\sqrt{s(9s-8)}}{2}, \tag{6}$$

$$\omega_z^2=s. \tag{7}$$

In $8/9<s<1$, the vertical frequency differs from both horizontal frequencies: substitution of $\lambda^2=-s$ into Eq. (1) gives $1-s\neq 0$. These linear results do not prove nonlinear stability.

4.2 Critical transitions

The four thresholds are

$$\kappa_1=\frac{c-1}{2}, \quad \kappa_R=\frac{c-\frac{8}{9}}{2},$$
$$\kappa_2=\frac{c}{2}, \qquad \kappa_3=\frac{1+2c}{4},$$

with $\kappa_1<\kappa_R<\kappa_2<\kappa_3$.

At κ_1, $B=0$. A zero eigenvalue pair occurs and the branches $Y^{\pm}$ emerge from C. The spatial stability window starts above this threshold.

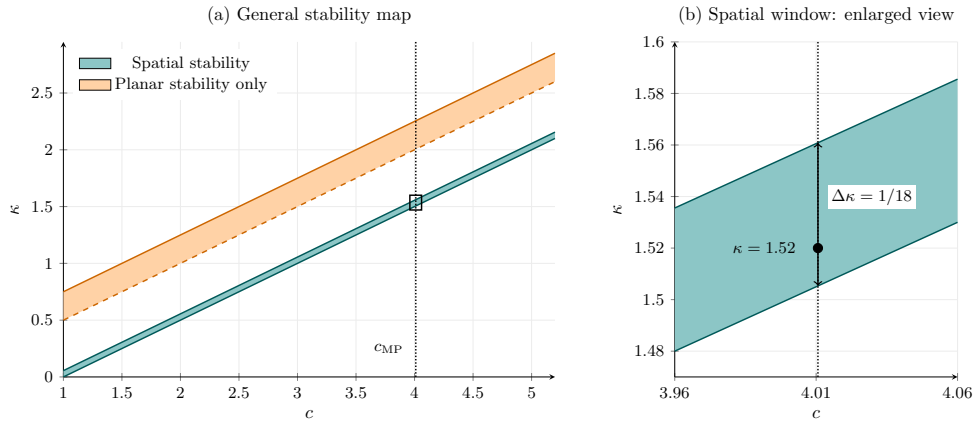


Fig. 2 Spectral stability of the central equilibrium in the unscreened model. The narrow lower band, $(c-1)/2 < \kappa < (c-8/9)/2$, gives bounded linearised motion in all three spatial directions. The upper band, $c/2 < \kappa < (c+1/2)/2$, has bounded planar motion but an unstable vertical mode. Outside these open bands, the central equilibrium does not have bounded linearised motion in the plane. The dotted line marks the Mars–Phobos curvature used in Section 5. Panel (b) enlarges the boxed region in panel (a), showing the spatial window of width 1/18 and the example $\kappa = 1.52$. No nonlinear confinement is implied by the shaded bands.

At κ_R, the two horizontal frequencies coincide at $\omega = \sqrt{5}/3$. Each eigenvalue $\pm i\omega$ has algebraic multiplicity two and geometric multiplicity one. The 1:1 frequency resonance is therefore non-semisimple, and the linearised solutions include secular terms. For $\kappa_R < \kappa < \kappa_2$, the horizontal spectrum is a complex quartet. This collision is the spectral setting for a possible Hamiltonian–Hopf bifurcation. Its nonlinear behaviour and any bifurcating periodic orbits require a resonant normal-form analysis.

At κ_2, the horizontal eigenvalues $\pm i$ are again double and non-semisimple. The vertical eigenvalue pair is zero. The branches $Z^{\pm}$ emerge, and C becomes vertically unstable. This simultaneous degeneracy requires a separate analysis in the spatial problem.

At κ_3, $A = 0$. A zero eigenvalue pair occurs and $X^{\pm}$ merge with C. The zero pairs at κ_1 and κ_3 are also non-semisimple. Thus, the endpoints are excluded when bounded linearised motion is required.

The equilibrium sequence is $3 \to 5 \to 7 \to 5$, as shown in the previous section. The second planar stability window is exactly the interval $\kappa_2 < \kappa < \kappa_3$, where all seven equilibria exist. The central equilibrium remains vertically unstable there.

4.3 Secondary equilibria

The *saddle index* denotes the number of real eigenvalue pairs. Hyperbolic directions give local stable and unstable manifolds; they do not by themselves prove global transport.

4.3.1 Transverse branches $Y^{\pm}$

The planar spectrum contains one real pair and one imaginary pair. Since

$$\Omega_{ZZ}(Y^{\pm}) = -1,$$

the spatial spectrum is

$$\pm\lambda, \qquad \pm i\omega, \qquad \pm i, \qquad \lambda, \omega > 0.$$

Thus, $Y^{\pm}$ are saddle–centre–centre equilibria of index one, with one stable and one unstable direction.

4.3.2 Longitudinal branches $X^{\pm}$

The planar spectrum is also of saddle–centre type. However,

$$\Omega_{ZZ}(X^{\pm}) = \frac{1 + (3 + 8c)X_s^2}{2(1 - X_s^2)} > 0.$$

The vertical mode adds a real pair $\lambda_z = \pm\sqrt{\Omega_{ZZ}(X^{\pm})}$. Hence, $X^{\pm}$ are saddle–saddle–centre equilibria of index two. Their spatial dynamics differs from that of $Y^{\pm}$.

4.3.3 Vertical branches $Z^{\pm}$

For $\kappa > c/2$, set

$$q_Z = 1 + Z_s^2 = \left(\frac{2\kappa}{c}\right)^{2/3} > 1.$$

The curvatures at $Z^{\pm}$ are

$$A_Z = 1 + 3c - \frac{3c}{q_Z}, \qquad \Omega_{YY} = 1,$$
$$\Omega_{ZZ} = -3c\frac{q_Z - 1}{q_Z} < 0.$$

The vertical mode is oscillatory. The horizontal equation is

$$\lambda^4 + (3 - A_Z)\lambda^2 + A_Z = 0, \tag{8}$$

with discriminant

$$\Delta_Z = (A_Z - 1)(A_Z - 9).$$

Since $A_Z > 1$, these branches are always unstable. For $1 < A_Z < 9$, the horizontal spectrum is a complex quartet. For $A_Z > 9$, it has two real pairs, giving saddle–saddle–centre equilibria of index two.

If $c > 8/3$, the transition occurs at

$$\boxed{\kappa_Z = \frac{c}{2}\left(\frac{3c}{3c-8}\right)^{3/2}}. \tag{9}$$

At κ_Z, $A_Z = 9$ and the horizontal eigenvalues are the repeated real values $\pm\sqrt{3}$; the equilibria remain unstable. Also, $\kappa_Z > \kappa_3$, so this transition occurs after $X^{\pm}$ have disappeared. If $1 < c \leq 8/3$, the complex quartet persists for every finite $\kappa > c/2$.

4.4 Dynamical implications

Only C has an open interval of spatial spectral stability. All secondary equilibria are unstable. The branches $Y^{\pm}$ have one real pair, whereas $X^{\pm}$ have an additional vertical instability. Their possible role in transport must be tested through invariant manifolds and the global dynamics. Linear stability alone does not establish confinement near C or access to its neighbourhood.

5 Application to the Mars–Phobos system

The local model is applied to the Mars–Phobos L_1 point. This example illustrates the equilibrium geometry and stability conditions of the previous sections.

5.1 Parameters and stability windows

The reference mass ratio and collinear coordinate are those adopted in the numerical study, based on Mars–Phobos data (Konopliv et al. 2006; Andert et al. 2010):

$$\mu = 1.661030656052 \times 10^{-8},$$
$$x_{L_1} = 0.998231928259.$$

The local curvature is

$$c = 4.010639624. \tag{10}$$

The spatial stability window of Section 4 is then

$$1.505319812 < \kappa < 1.560875368. \tag{11}$$

The second planar window is

$$2.005319812 < \kappa < 2.255319812. \tag{12}$$

Its central equilibrium is vertically unstable. The displayed endpoints are rounded; the exact bounds are those derived in Section 4.

5.2 Two representative regimes

The comparison uses $\kappa = 1.52$ in the spatial window and $\kappa = 2.1$ in the upper planar window. Table 1 gives the positive branch coordinates in units of the source half-separation ℓ.

Table 1 Equilibria and central spectral stability for two parameter values. The negative branches follow by reflection.

Quantity	$\kappa = 1.52$	$\kappa = 2.1$
X_s	0.423140725	0.187211887
Y_s	0.080566423	0.498512539
Z_s	—	0.176730607
Number of equilibria	5	7
Planar stability of C	stable	stable
Vertical stability of C	stable	unstable

The lower-window case has spatial spectral stability, but $Y^{\pm}$ lie close to the centre. The upper-window case gives greater transverse separation. However, its central vertical curvature is

$$D = -c + 2\kappa = 0.189360376 > 0.$$

It also contains $Z^{\pm}$. Thus, the five planar equilibria do not describe the full spatial configuration.

5.3 Dimensional scale and clearance

To retain the scale of the extended study, take $\ell = 12.2435\,\mathrm{m}$. The distances from the centre are then

κ	$d_X = \ell X_s$	$d_Y = \ell Y_s$
1.52	5.181 m	0.986 m
2.1	2.292 m	6.104 m

For a central exclusion radius $R_{\mathrm{safe}} = 2\,\mathrm{m}$, only $X^{\pm}$ lie outside the excluded region in the lower-window case. All four planar secondary points lie outside it for $\kappa = 2.1$. Their clearance does not imply that complete approach trajectories avoid the spacecraft, electrodes or supports. A solid central ball also excludes C; access to its neighbourhood requires a different material layout.

An illustrative charge scale follows from the isolated-sphere relation $Q \simeq 4\pi\varepsilon_0 RV$. Let the source and sample radii be $R_O = 1\,\mathrm{m}$ and $R_C = 0.5\,\mathrm{m}$, with sample mass $m = 10\,\mathrm{kg}$. For voltages of the same sign,

$$\kappa \simeq \frac{4\pi\varepsilon_0 R_O R_C |V_O V_C|}{m n^2 \ell^3}. \tag{13}$$

With $|V_O| = |V_C| = 6\,\mathrm{kV}$, the adopted scale at $\kappa = 2.1$ implies $n \simeq 2.27954 \times 10^{-4}\,\mathrm{s}^{-1}$. This reproduces the illustrative scaling of the extended study; it is not an independent

estimate of the orbital mean motion. At fixed ℓ, the lower-window case requires a smaller charge product. These values do not establish hardware feasibility. Mutual capacitance requires separate assessment. Section 5.7 examines plasma screening at fixed prescribed charges.

5.4 Critical levels and local spectra

The original numerical calculation used the total separation $L = 2\ell$ as its length unit. To compare its results with the present model, define

$$u = X/2, \qquad v = Y/2, \qquad \Sigma = \kappa/8.$$

In the plane $Z = 0$, the corresponding potential is

$$\begin{aligned} W(u,v) = {} & \tfrac{1}{2}[(1+2c)u^2 + (1-c)v^2] \\ & - \frac{\Sigma}{\sqrt{(u+1/2)^2+v^2}} \\ & - \frac{\Sigma}{\sqrt{(u-1/2)^2+v^2}}. \end{aligned} \tag{14}$$

Thus, $\Omega(2u, 2v, 0) = 4W(u, v)$ and

$$\mathcal{C}_L = 2W - u'^2 - v'^2, \qquad \mathcal{C}_\ell = 4\mathcal{C}_L. \tag{15}$$

Time remains scaled by n^{-1}.

For $\kappa = 2.1$, or $\Sigma = 0.2625$, the critical values in total-separation units are

$$\begin{aligned} \mathcal{C}_{L,C} &= -2.100000000, \\ \mathcal{C}_{L,X} &= -2.097229604, \\ \mathcal{C}_{L,Y} &= -2.066461081. \end{aligned} \tag{16}$$

The planar spectra are

	Real pair	Imaginary pair
$X^\pm$	± 0.852954	$\pm 1.970497\,i$
$Y^\pm$	± 1.574536	$\pm 1.865251\,i$

Both branches have saddle–centre structure in the plane. Their spatial types remain different, as shown in Section 4. The critical Jacobi levels describe changes in the planar allowed set $2W - \mathcal{C}_L \geq 0$. They are not control costs or evidence of long-term confinement.

Figure 3 gives a geometric interpretation of these levels for the unscreened model. The white area satisfies $2W - \mathcal{C}_L \geq 0$, so the energy condition permits motion there. The grey area is forbidden because it would require a negative squared speed. As $\mathcal{C}_L$ increases above $\mathcal{C}_{L,C}$, a forbidden region appears around the centre. At $\mathcal{C}_{L,X}$, it

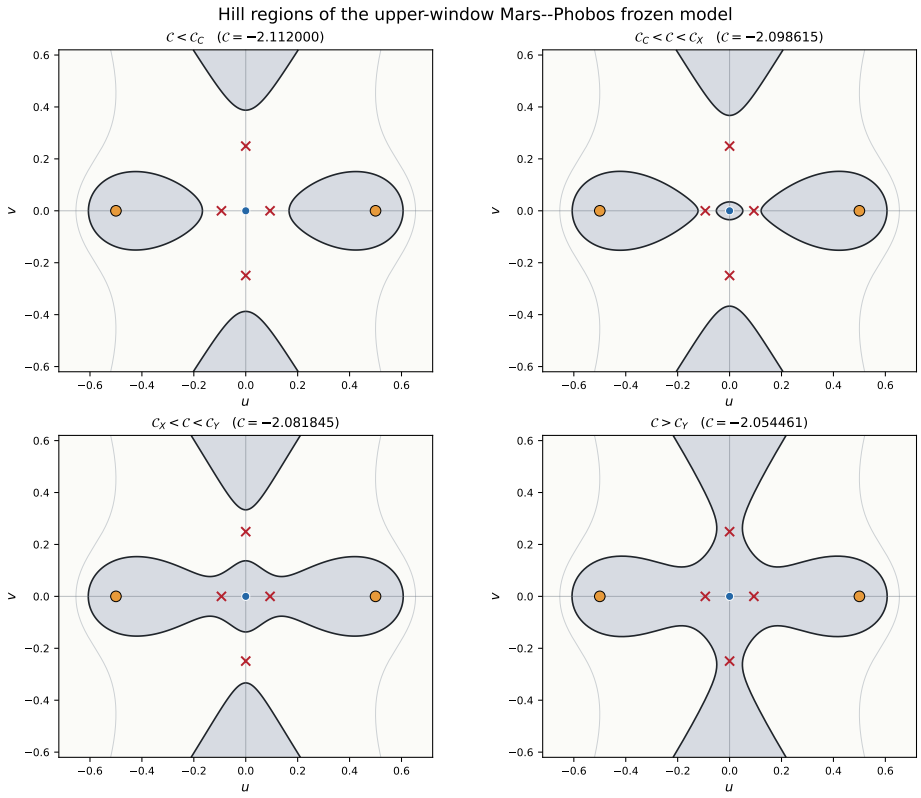


Fig. 3 Planar Hill regions for the unscreened Mars–Phobos example with $c = 4.010639624$ and $\kappa = 2.1$ ($\Sigma = 0.2625$). Coordinates use the total source separation $L = 2\ell$. In the panel headings, $\mathcal{C}$ denotes $\mathcal{C}_L$, and the subscripts C, X and Y denote its critical equilibrium values. White is energetically allowed, grey is forbidden, and black curves are zero-velocity boundaries. Orange circles mark the point sources; the blue point marks C, and red crosses mark $X^{\pm}$ and $Y^{\pm}$. The blue marker identifies the centre and does not indicate spatial stability: this example has an unstable vertical mode. Electrode sizes and the central physical exclusion region are not shown.

joins the forbidden regions around the sources. The next transition, at $\mathcal{C}_{L,Y}$, joins this region to the upper and lower forbidden areas. Thus, the sequence shows changes in the available passages, rather than a closed region that traps the capsule near C.

These are planar cuts of an energy constraint. They do not establish which passages a trajectory will follow, or whether a spatial path can leave the plane. The central exclusion radius discussed above is a separate geometric restriction and is not included in this shading.

5.5 A local periodic orbit

A small planar Lyapunov orbit near Y^{+} gives a numerical check of the local dynamics. In total-separation units, symmetry shooting fixes $v_0 = Y_s/2 - 10^{-3}$ and solves

$u(T/2) = v'(T/2) = 0$. The corrected initial state and period are

$$\begin{aligned} u_0 &= v_0' = 0, \\ v_0 &\simeq 0.248256269632644, \\ u_0' &\simeq -0.000840292164379, \\ T &\simeq 3.368555157541, \\ \mathcal{C}_L &\simeq -2.066463580254. \end{aligned}$$

The hyperbolic Floquet multipliers of the planar variational system are

$$\rho_u \simeq 201.111234491, \qquad \rho_s \simeq 0.004972372640,$$

with the other two planar multipliers close to unity. The vertical Floquet pair is not computed here. Using the archived full-precision state, DOP853 with relative and absolute tolerances 2.3×10^{-14} and 10^{-15} gives a closure error of 9.1×10^{-15}. A separate 40-digit Wolfram integration supports the orbit and its hyperbolic multipliers. Rounded initial data need not reproduce the same closure error.

The displacement used in shooting is about 2.45 cm and the period is about 4.105 h under the illustrative scaling. This orbit confirms a local periodic solution. It does not establish global transport, spatial confinement or controlled capture.

5.6 Influence of higher-order gravitational terms

The local gravitational approximation is tested by retaining the third- and fourth-order terms of the CR3BP potential. These add quadratic and cubic terms to the equations of motion; the electrostatic potential is kept unchanged. Let $d_j = x_{L_i} - x_j$ be the signed distance from the reference point to primary j, in units of a, and let $m_1^* = 1 - \mu$, $m_2^* = \mu$. The third-order local potential is

$$\begin{aligned} \Omega^{(3)} &= \Omega + \beta \left[X^3 - \tfrac{3}{2} X (Y^2 + Z^2) \right], \\ \beta &= -\frac{\ell}{a} \sum_{j=1}^{2} \frac{m_j^* \operatorname{sgn}(d_j)}{|d_j|^4}. \end{aligned} \tag{17}$$

Writing $R_\perp^2 = Y^2 + Z^2$, the fourth-order approximation is

$$\begin{aligned} \Omega^{(4)} &= \Omega^{(3)} + \gamma \left[X^4 - 3X^2 R_\perp^2 + \tfrac{3}{8} R_\perp^4 \right], \\ \gamma &= \left(\frac{\ell}{a} \right)^2 \sum_{j=1}^{2} \frac{m_j^*}{|d_j|^5}. \end{aligned} \tag{18}$$

Here Ω is the quadratic-gravity, two-source potential. At L_1, $d_1 > 0$ and $d_2 < 0$. The illustrative circular separation $a = 9378$ km (NASA Goddard Space Flight Center n.d.) gives $\beta = 0.00221785119$, $\gamma = 1.63866359 \times 10^{-6}$ and $\ell / R_{2,L_1} = 7.3841 \times 10^{-4}$.

For this comparison, x_{L_1} and c are recomputed from the adopted mass ratio at high precision, avoiding a residual force from rounded coordinates.

Both added terms have zero gradient and zero Hessian at the origin. Consequently, C remains an equilibrium and its linear spectrum is unchanged. This also holds for the full CR3BP gravitational potential with the same symmetric, prescribed electric sources. Thus, the central spectral stability intervals do not arise from discarding these terms. They do affect the nonlinear equations near C, so this statement concerns linear stability, not nonlinear confinement.

Away from the centre, the cubic term breaks reflection symmetry in X. The longitudinal points are no longer equally spaced about C, and the transverse and vertical branches acquire a small longitudinal displacement. For example, at $\kappa = 1.52$ without screening, the longitudinal coordinates become -5.178870 and $5.182577\,\mathrm{m}$. The transverse pair shifts by $0.08645\,\mathrm{mm}$ in the positive longitudinal direction. Reflections in Y and Z are preserved.

Table 2 compares the continued equilibria with those of the full gravitational potential. It also includes the screened cases defined in Section 5.7. The largest cubic displacement is about $2.18\,\mathrm{mm}$, while the largest difference between cubic and full-gravity positions is about $2.07\,\mu\mathrm{m}$. Including the fourth-order term reduces the largest position error to $0.358\,\mathrm{nm}$. This is a truncation error within the same idealised model, not an estimate of physical positioning accuracy. All continued equilibria retain their spectral type in these cases. This supports the local approximation at the adopted scale, away from degenerate thresholds. It does not prove that the truncated and full models have identical global equilibrium sets or trajectories.

Table 2 Maximum equilibrium position errors relative to the full CR3BP gravitational model, with the same electric field. $\Delta_{F,3}$ and $\Delta_{F,4}$ compare full-gravity positions with the third- and fourth-order approximations, respectively. Maxima are over the continued branches in each case.

κ	λ_D (m)	$\Delta_{F,3}$ (μm)	$\Delta_{F,4}$ (nm)
1.52	∞	0.773	0.302
2.10	∞	2.074	0.358
1.52	45	0.773	0.302
1.60	45	0.744	0.274

5.7 Effect of screening on the Mars–Phobos equilibrium geometry

This subsection examines how plasma screening changes the equilibrium geometry near the Mars–Phobos L_1 point. The illustrative screening length $\lambda_D = 45\,\mathrm{m}$ follows Aslanov (Aslanov 2021b), who adopted it without a measured value at L_1. The model retains the two repulsive sources and uses a smooth Debye–Hückel potential. This is a

sensitivity model: an effective screening length requires calibration to the plasma and charging regime (Seubert et al. 2014).

With fixed charges and a uniform screening length, the effective potential is

$$\begin{aligned}\Omega_D &= \tfrac{1}{2}[(1+2c)X^2 + (1-c)Y^2 - cZ^2] \\ &\quad - \kappa \sum_{\sigma=\pm} \frac{e^{-\delta_D \rho_\sigma}}{\rho_\sigma}, \qquad \delta_D = \frac{\ell}{\lambda_D}.\end{aligned} \tag{19}$$

Here $\rho_\pm^2 = (X \mp 1)^2 + Y^2 + Z^2$. For $c = 4.010639624$, $\ell = 12.2435\,\mathrm{m}$ and $\lambda_D = 45\,\mathrm{m}$, the screening parameter is $\delta_D = 0.272078$. The positive longitudinal and transverse coordinates are computed from

$$\begin{aligned}(1+2c)X + \kappa[H_D(1+X) - H_D(1-X)] &= 0, \\ 2\kappa G_D\left(\sqrt{1+Y^2}\right) &= c - 1,\end{aligned} \tag{20}$$

where $G_D(r) = e^{-\delta_D r}(1+\delta_D r)/r^3$ and $H_D(r) = rG_D(r)$, with $0 < X < 1$ and $Y > 0$. The central point remains fixed by symmetry.

Table 3 Effect of screening and charge adjustment at the adopted Mars–Phobos scale. Distances are measured from the source midpoint; the negative branches follow by reflection.

	Coulomb	Screened	Screened
κ	1.52	1.52	1.60
d_X (m)	5.181	5.192	4.875
d_Y (m)	0.986	—	1.711
Equilibria	5	3	5
C spectrally stable	yes	no	yes

At fixed $\kappa = 1.52$, screening moves each longitudinal equilibrium outward by only 1.10 cm, but removes the transverse pair (Table 3). As λ_D decreases, this pair contracts towards C and merges with it at $\lambda_D \simeq 83.94\,\mathrm{m}$, obtained by setting $Y = 0$ in Eq. (20). Thus the adopted 45 m case has three equilibria instead of five. Neither vertical nor non-axial equilibria occur in the three cases shown.

At 45 m, the transverse pair reappears for $\kappa > 1.553377$. Increasing the charge product by 5.26%, to $\kappa = 1.60$, places it at $d_Y = 1.711\,\mathrm{m}$ and restores central spectral stability, as checked from the spatial linearisation. Its distance remains below the illustrative 2 m exclusion radius. Screening therefore changes both the number and spacing of the equilibria; charge adjustment recovers a five-point configuration but does not by itself establish clearance or capture.

6 Discussion

6.1 Physical interpretation

The unscreened model separates source geometry from the local gravitational curvature. It provides explicit equilibrium branches and stability thresholds. The planar picture does not describe all spatial effects: $X^{\pm}$ have an unstable vertical mode, and $Z^{\pm}$ exist above $\kappa = c/2$. Even in the lower stability window, a purely imaginary spectrum does not prove nonlinear confinement. Resonances and finite excursions require further analysis.

The sources have fixed charges and prescribed positions in the rotating frame. The sample is a test particle. Spacecraft recoil, attitude motion and station-keeping are omitted. The screening calculation in Section 5.7 shows that the transverse pair can disappear even when the longitudinal displacement is small. Its adopted screening length still requires calibration to the local plasma conditions. These effects limit the physical interpretation of the numerical example.

Finite conductors require a geometry-dependent capacitance model; fixed voltage is not equivalent to fixed charge. The Multi-Sphere Method provides one possible extension (Stevenson and Schaub 2013). The isolated sphere values in Section 5 only give a dimensional scale. They do not establish voltage, power or operational requirements.

6.2 A small charge asymmetry

The symmetric model fixes C at the midpoint of the sources. To move this equilibrium, let $\kappa_{\pm} = \kappa \pm \delta$, with $|\delta|$ small. The longitudinal equilibrium equation near the origin is

$$0 = -2\delta + (1 + 2c - 4\kappa)\Delta X + O(\delta^2).$$

Provided $1 + 2c - 4\kappa \neq 0$,

$$\Delta X = \frac{2\delta}{1 + 2c - 4\kappa} + O(\delta^2). \tag{21}$$

This gives a local displacement mechanism. Near the longitudinal bifurcation, nonlinear continuation is needed. Any displaced equilibrium must also be checked against the spacecraft exclusion geometry.

6.3 Transport and capture

The Jacobi integral is conserved and the Hamiltonian flow preserves phase volume. The frozen field therefore cannot produce an asymptotically stable equilibrium with an open basin. Stable manifolds allow asymptotic approach from lower-dimensional sets, but this does not imply capture of an open set of initial conditions.

A prescribed time-dependent potential can change energy while still preserving phase volume. Such modulation may support insertion into a selected state or orbit. Asymptotic settling requires a dissipative or closed-loop mechanism that produces contraction. Global manifold connections, collision clearance and controlled insertion remain separate problems.

7 Conclusions

A symmetric pair of repulsive electrostatic sources changes the local equilibrium structure near a collinear libration point. The unscreened model has explicit longitudinal, transverse and vertical branches. Their bifurcations give the sequence $3 \to 5 \to 7 \to 5$ as the charge strength increases.

The central equilibrium has an open spatial spectral-stability window of width 1/18. Its upper boundary is a non-semisimple frequency collision. A possible Hamiltonian–Hopf bifurcation requires further nonlinear analysis. All secondary equilibria are spatially unstable: $Y^{\pm}$ have one real pair, $X^{\pm}$ have two, and $Z^{\pm}$ have a complex quartet or two real pairs.

The Mars–Phobos example shows the trade-off between spatial spectral stability and transverse separation. At the adopted screening length, the nominal transverse pair disappears; a modest increase in the charge product restores a five-point configuration and central spectral stability. A corrected Lyapunov orbit in the unscreened model supports the local periodic dynamics. Comparisons with the full CR3BP gravitational potential show small changes in the secondary equilibrium positions at the adopted scale. The central linear spectrum is unchanged by higher-order gravitational terms for the same symmetric, prescribed sources. The results do not establish long-term confinement or capture. Further work should address the resonant dynamics, orbit continuation in the full gravitational field, finite conductors and a physically constrained insertion mechanism.

References

Aliasi G, Mengali G, Quarta AA (2011) Artificial equilibrium points for a generalized sail in the circular restricted three-body problem. Celestial Mechanics and Dynamical Astronomy 110(4):343–368. https://doi.org/10.1007/s10569-011-9366-y

Andert TP, Rosenblatt P, Pätzold M, et al (2010) Precise mass determination and the nature of Phobos. Geophysical Research Letters 37(9):L09202. https://doi.org/10.1029/2009GL041829

Aslanov V, Schaub H (2019) Detumbling attitude control analysis considering an electrostatic pusher configuration. Journal of Guidance, Control, and Dynamics 42(4):900–909. https://doi.org/10.2514/1.G003966

Aslanov VS (2021a) Prospects of Phobos sample return mission using electrostatic container. Journal of Spacecraft and Rockets 58(6):1799–1805. https://doi.org/10.2514/1.A34984

Aslanov VS (2021b) A splitting of collinear libration points in circular restricted three-body problem by an artificial electrostatic field. Nonlinear Dynamics 103:2451–2460. https://doi.org/10.1007/s11071-021-06226-4

Bombardelli C, Peláez J (2011) On the stability of artificial equilibrium points in the circular restricted three-body problem. Celestial Mechanics and Dynamical

Astronomy 109(1):13–26. https://doi.org/10.1007/s10569-010-9317-z

Conley CC (1968) Low energy transit orbits in the restricted three-body problems. SIAM Journal on Applied Mathematics 16(4):732–746. https://doi.org/10.1137/0116060

Konopliv AS, Yoder CF, Standish EM, et al (2006) A global solution for the Mars static and seasonal gravity, Mars orientation, Phobos and Deimos masses, and Mars ephemeris. Icarus 182:23–50. https://doi.org/10.1016/j.icarus.2005.12.025

Koon WS, Lo MW, Marsden JE, et al (2001) Low energy transfer to the moon. Celestial Mechanics and Dynamical Astronomy 81(1–2):63–73. https://doi.org/10.1023/A:1013359120468

McInnes CR, McDonald AJC, Simmons JFL, et al (1994) Solar sail parking in restricted three-body systems. Journal of Guidance, Control, and Dynamics 17(2):399–406. https://doi.org/10.2514/3.21211

NASA Goddard Space Flight Center (n.d.) Mars fact sheet. https://nssdc.gsfc.nasa.gov/planetary/factsheet/marsfact.html, accessed 22 September 2026; Phobos semimajor axis: 9378 km

Richardson DL (1980) Analytic construction of periodic orbits about the collinear points. Celestial Mechanics 22(3):241–253. https://doi.org/10.1007/BF01229511

Schaub H, Parker GG, King LB (2004) Challenges and prospects of coulomb spacecraft formation control. The Journal of the Astronautical Sciences 52(1–2):169–193. https://doi.org/10.1007/BF03546427

Seubert CR, Stiles LA, Schaub H (2014) Effective Coulomb force modeling for spacecraft in earth orbit plasmas. Advances in Space Research 54:209–220. https://doi.org/10.1016/j.asr.2014.04.005

Stevenson D, Schaub H (2013) Multi-sphere method for modeling spacecraft electrostatic forces and torques. Advances in Space Research 51(1):10–20. https://doi.org/10.1016/j.asr.2012.08.014

Statements and Declarations

Funding

The authors received no financial support for the research, authorship or publication of this article.

Competing Interests

The authors have no relevant financial or non-financial interests to disclose.

Data Availability

No external datasets were used in this study. The numerical data supporting the findings of this study are available from the corresponding author upon reasonable request.